
First-Principles Investigations on Ionization and Thermal Conductivity of Polystyrene (CH) for Inertial Confinement Fusion Applications

Introduction

Controlled inertial confinement fusion (ICF) has been pursued in laboratories for decades, in both indirect-drive^{1–3} and direct-drive^{4–6} schemes. A typical ICF target consists of layered solid deuterium–tritium (DT) covered with an ablator layer.⁷ The ablator layer is used to convert the laser and/or x-ray energy to the kinetic energy of the imploding shell (besides compressing it) by the rocket effect through the ablation process. Polystyrene (CH) is often chosen as the ablator material⁷ since it is inexpensive and easy to make. Upon x-ray or laser ablation, the CH ablator can be shocked to pressures up to tens of Mbars. The target convergence can further bring the CH-layer pressure to Gbars, or even hundreds of Gbars at peak compression. Besides ICF applications, CH is also often used as an effective ablator for high-energy-density–physics (HEDP) experiments.^{8–10} The properties of CH plasmas under such high-energy-density conditions are essential for understanding ICF and HEDP experiments involving CH ablators.

Because of its importance to ICF, the plasma properties of polystyrene have been extensively studied in both experiment and theory. For example, the principal Hugoniot of CH has been measured using gas-gun experiments¹¹ and laser/x-ray-launched shocks.^{12–16} The measured pressures, temperatures, and reflectivity of shocked CH compare well with state-of-the-art calculations using first-principles methods^{17–19} along the principal Hugoniot. The original *SESAME* model (Table 7593 for CH) gave a reasonable Hugoniot in the pressure range that experiments explored, while it overestimated the Hugoniot temperatures.^{18,19} Off the principal Hugoniot, we calculated the equations of state over a wide range of CH-plasma conditions and constructed a first-principles equation-of-state (FPEOS) table of CH for ICF applications. The FPEOS of CH has shown significant differences for warm-dense-plasma conditions¹⁹ when compared to the original *SESAME* model. Its effect on ICF implosions has been examined in hydrodynamic simulations: a smaller mass ablation rate was predicted with the CH FPEOS. This prompts us to consider other plasma properties

such as ionization and thermal conductivity that can be self-consistently extracted from such first-principles calculations for ICF and HEDP applications.

Thermal conductivity (κ) is an important plasma property that is needed in ICF simulations because it determines the heat transport in ICF plasmas and affects the hydrodynamic instability growth in ICF implosions.²⁰ In traditional ICF simulations, plasma-physics models of thermal conductivity were adopted in hydrocodes. For example, the Spitzer model²¹ has been extensively used for classical plasmas. However, such an analytical model breaks down in warm-dense-plasma conditions since the Spitzer Coulomb logarithm becomes negative for low-temperature and high-density plasmas. To overcome this difficulty of computing κ for warm dense plasmas, the Lee–More model²² was developed in the 1980s with the first-order approximation to the Boltzmann equation. The Purgatorio model²³ and the SCAALP model,²⁴ developed about a decade ago, are both based on the average atom model. In the past, quantum-molecular dynamics (QMD) calculations of κ have been performed for ICF-relevant materials of deuterium^{25–29} and CH/CH₂ (Refs. 30–32). These first-principles calculations have indicated a larger κ for warm dense D₂ and CH plasmas than the predictions of the Lee–More model that was widely adopted in hydrocodes for ICF simulations. These QMD calculations, however, have been performed for only a few specific density–temperature conditions of CH plasmas. To test whether or not such an enhanced κ of CH will affect ICF simulations, one must extend such QMD calculations to a wide range of plasma conditions, similar to the deuterium case in Ref. 29. In this article, we report on such an endeavor to “gauge” the global behavior of CH thermal conductivity from direct QMD calculations of κ for a wide range of CH plasma conditions. The obtained analytical form of κ , fitted with the generalized QMD Coulomb logarithm, has then been used in hydrodynamic simulations to explore its effect in ICF implosions. Our results show that the κ_{QMD} simulations give an ~20% variation in neutron yield and peak hot-spot pressure when compared to the use of the traditional Lee–More model.

A brief description of the QMD method is presented that combines the orbital-based Kohn–Sham molecular dynamics (KSMD) method with the orbital-free molecular dynamics (OFMD). Since all physics models of the thermal conductivity invoked the use of an effective ionic charge in single-fluid ICF simulations, we first present the OFMD calculations of the average ionization ($\langle Z \rangle$ and $\langle Z^2 \rangle$) of CH over a wide range of plasma densities and temperatures. The obtained $\langle Z \rangle$ and $\langle Z^2 \rangle$ are then fitted with a Saha-type model, while the KSMD-derived thermal conductivities of CH are compared with the Lee–More model and fitted with the generalized Coulomb logarithm [$\ln\Lambda$]_QMD. The κ_{QMD} effects on ICF implosions for both OMEGA and National Ignition Facility (NIF) targets are presented, followed by the conclusions.

The Quantum-Molecular Dynamics Method

The QMD method is an effective first-principles method for simulating warm dense plasmas,^{33–36} where quantum mechanics is used to describe the dynamics of electrons in combination with classical molecular dynamics for the ion motion. To make the quantum-mechanical computations of a many-electron system feasible, the traditional QMD method is based on the density functional theory (DFT).^{37–39} Depending on the choice of DFT implementation, the QMD method can be either orbital based or orbital free. For instance, the KSMD method uses the plane-wave basis in a finite-temperature DFT format, which has been implemented in the Vienna *ab-initio* simulation package (VASP),^{40–42} while the OFMD method⁴³ represents the electronic free energy as a direct function of the electronic density through a semiclassical expansion of the Mermin functional. The KSMD method can handle dense plasmas, but only up to the Fermi temperature; the large number of basis functions needed for high- T plasmas renders KSMD as computationally impractical. In contrast, the OFMD method is suitable for high- T plasma simulations. Combining the two first-principles methods of KSMD and OFMD, we are able to simulate a wide range of plasma conditions. Since both methods have been documented elsewhere, only a brief description follows.

1. KSMD

The KSMD method implemented in VASP is based on the finite-temperature density functional theory (FTDFT). To be specific, the electrons are treated quantum-mechanically by plane-wave FTDFT calculations using the Perdew–Burke–Ernzerhof exchange-correlation functional⁴⁴ in the generalized gradient approximation. The electron–ion interaction is modeled by a projector-augmented wave (PAW) pseudopotential. The system was assumed to be in local thermodynamical equilibrium with equal electron and ion temperatures ($T_e = T_i$).

The ion temperature was kept constant through simple velocity scaling during a molecular-dynamics simulation.

A periodically replicated cubic cell is used with equal numbers of C and H atoms. The plasma density and the number of atoms determine the volume of the cell. For the present simulations of densities below $\rho = 17.5 \text{ g/cm}^3$, we have employed 250 atoms in total, while a total of 432 atoms were used for densities of $\rho \geq 25 \text{ g/cm}^3$. For each molecular-dynamics (MD) step, a set of electronic-state functions for each k point is self-consistently determined for an ionic configuration. Under the Born–Oppenheimer approximation, the ions are moved classically with a velocity Verlet algorithm, according to the combined ionic and electronic forces. Repeating the two steps propagates the system in time, resulting in a set of self-consistent ion configurations and electronic-state functions. These trajectories provide a consistent set of static, dynamic, and optical properties of the simulated CH plasmas.

The Γ -point sampling of the first Brillouin zone in the cubic cell was employed and tested with a $2 \times 2 \times 2$ Monkhorst–Pack k -point grid. It was found that the resulting thermal conductivity varies $<5\%$. To converge the plasma property calculations, the plane-wave cutoff energy was set to $E_{\text{max}} = 1000 \text{ eV}$ and the PAW potentials were adopted with tight cores (core radii of 1.1 and 0.8 atomic units for C and H, respectively). A large number of energy bands (up to $N_b = 11,000$) have been included to ensure that the population of the highest energy band is $<10^{-4}$. For the lowest temperature, 500 bands and a time step of $\Delta t = 0.5 \text{ fs}$ were used, while at the highest temperature, a larger number of bands (11,000) and a small time step of $\Delta t = 0.011 \text{ fs}$ were used.

To calculate the electronic thermal conductivity of CH plasmas, the linear response of the plasma to an electric field \mathbf{E} and a temperature gradient ∇T are considered, which induce the electric current \mathbf{j}_e and the heat flux \mathbf{j}_q :

$$\mathbf{j}_e = \left(eL_{11}\mathbf{E} - \frac{L_{12}\nabla T}{T} \right) / e, \quad (1)$$

$$\mathbf{j}_q = \left(eL_{21}\mathbf{E} - \frac{L_{22}\nabla T}{T} \right) / e. \quad (2)$$

For plasmas having no electric current ($\mathbf{j}_e = 0$), the above equations in combination with the definition of $\mathbf{j}_q = -\kappa\nabla T$ give the thermal conductivity

$$\kappa = \frac{1}{T} \left(L_{22} - \frac{L_{12}^2}{L_{11}} \right) \quad (3)$$

with the Onsager coefficients given by $L_{ij} \equiv L_{ij}(0)$. The frequency-dependent Onsager coefficients can be calculated using the Kubo–Greenwood formalism^{45,46}

$$L_{ij}(\omega) = \sum_{mn} \frac{2\pi(-e)^{4-i-j}}{3Vm_e^2\omega} F_{mn} |D_{mn}|^2 \\ \times \left(\frac{E_m + E_n}{2} - H \right)^{i+j-2} \delta(E_m - E_n - \hbar\omega), \quad (4)$$

where V is the atomic volume, E_m (E_n) is the energy of the m th (n th) state, and H is the enthalpy (per atom) of the system. F_{mn} is the difference between the Fermi–Dirac distributions for the involved states m and n at temperature T . The velocity matrix elements D_{mn} can be evaluated from the VASP wave functions. In practical calculations, the δ function in Eq. (4) is approximated by a Gaussian function of width ΔE (≈ 0.1 to 0.5 eV). The resulting κ was averaged over at least five snapshots of uncorrelated configurations along the MD trajectories. The convergence of κ required a much larger number of energy bands (~ 2 to $3\times$) than for the MD simulation.

2. OFMD

The development of OFMD has been documented elsewhere.⁴³ In the OFMD method, the free energy is approximated by a direct function of the electronic density through a semiclassical expansion of the Mermin functional. The leading- and next-to-leading-order expansions, in terms of the Planck constant \hbar , give the well-known finite-temperature Thomas–Fermi model. To preserve the electronic density beyond the cutoff radius, the OFMD method has introduced a norm-conserving regularization by imposing an analytical form to the electronic density within the cutoff volume. The local-density approximation (LDA) has been used for the electron exchange correlation functional in our OFMD simulations. The time steps used in these calculations vary from 2.4×10^{-2} fs to 4.8×10^{-3} fs, depending on the density and temperature of the CH plasma. The pressures calculated from both KSMD and OFMD methods at the temperature “boundary” of $T \simeq T_F$ are matched well (within $<1\%$).

Since the OFMD method is not based on the plane-wave orbital expansion, it does not give wave functions as in KSMD; therefore, the transport properties of plasmas at high temperatures cannot be extracted directly from the current OFMD simu-

lations. The OFMD method is used to calculate the static plasma properties such as pressure and internal energy. The OFMD simulations can be used to estimate the average ionization in CH plasmas. It is noted that all electrons (core and valence) are considered in the OFMD method. Although there is no operator for ionization in a quantum many-body system, the concept of average ionization ($\langle Z \rangle$ and $\langle Z^2 \rangle$) is extensively adopted in plasma physics models. To fit our KSMD-calculated thermal-conductivity results with a generalized Coulomb logarithm for its use in hydrocodes, we must apply the OFMD calculations to obtain $\langle Z \rangle$ and $\langle Z^2 \rangle$ for a wide range of plasma conditions.

The OFMD calculations give the total pressure of CH plasmas. As described in previous references,^{30,47} one can use the orbital-free average atom model in conjunction with the pressure-matching mixing rule to calculate the average charge states for C and H atoms, respectively. For the case of LDA exchange correlation, the pressure matching is equivalent to equalizing the free-electron density of C and H atoms. Once the effective charge states Z_C and Z_H are obtained, the average ionization quantities of $\langle Z \rangle$ and $\langle Z^2 \rangle$ of CH plasmas can be computed as follows (as defined in our hydrocodes):

$$\langle Z \rangle = (Z_C + Z_H)/2, \quad (5)$$

$$\langle Z^2 \rangle = (Z_C^2 + Z_H^2)/2, \quad (6)$$

for an equal mixture of C and H atoms. The effective charge extensively used in hydrocodes is $Z_{\text{eff}} = \langle Z^2 \rangle / \langle Z \rangle$.

Results and Discussions

1. The Average Ionization $\langle Z \rangle$ and $\langle Z^2 \rangle$ of CH

As described above, the OFMD method was used to estimate the average ionization of $\langle Z \rangle$ and $\langle Z^2 \rangle$ for CH plasmas of densities varying from $\rho = 0.01$ g/cm³ to $\rho = 100$ g/cm³ and temperatures of $T \simeq 10.8$ to 344.7 eV. As an example, Fig. 145.20 shows the comparison of $\langle Z \rangle$ as a function of CH density between the OFMD prediction and the Astrophysics Opacity Table (AOT)⁴⁸ for two plasma temperatures of $T \simeq 10.8$ eV and $T \simeq 86.2$ eV. It is noted that the AOT model, usually patched with cold opacity in the warm-dense-plasma regime, is currently adopted in our hydrocodes for ICF simulations.⁴⁹ Figure 145.20 shows that at relatively low densities ($\rho < 1$ g/cm³), the AOT model gives similar values of $\langle Z \rangle$ as the OFMD calculation for both temperatures, while significant differences are seen for higher densities at both temperatures. For instance, at $T \simeq 86.2$ eV

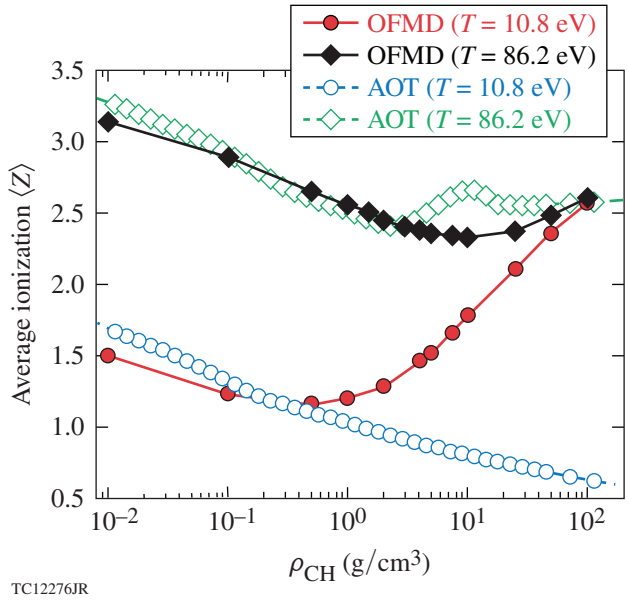


Figure 145.20

The orbital-free molecular dynamics (OFMD)–predicted average ionization $\langle Z \rangle$ as a function of CH density for two plasma temperatures of $T \simeq 10.8$ eV and $T \simeq 86.2$ eV, which are compared with the model predictions (open symbols) by the Astrophysics Opacity Table (AOT) currently used in our hydrocodes.

there are discrepancies in $\langle Z \rangle$ between AOT and OFMD for densities around $\rho = 10$ g/cm³. Drastic differences are found for the case of a lower temperature at $T \simeq 10.8$ eV: the cold-opacity-patched AOT model does not give the correct behavior of pressure ionization when the CH density increases, which is in contrast to the OFMD prediction. Since low-temperature CH plasma conditions ($T \leq 10$ eV) are often encountered in ICF implosions,¹⁹ it is important that the correct $\langle Z \rangle$ be used for the thermal conductivity models in hydrocodes.

As discussed above, the average ionization of CH plasmas was calculated over a wide range of densities for four different temperatures of $T \simeq 10.8$ eV, 21.6 eV, 86.2 eV, and 344.7 eV. The resulting $\langle Z \rangle$ and $\langle Z^2 \rangle$ are plotted in Figs. 145.21 and 145.22 as open symbols. To use these average-ionization quantities in hydrocodes for ICF simulations, a “Saha-type” ionization model for CH plasmas was derived in which the average-ionization fraction ξ is defined as

$$\frac{\xi^2}{1-\xi} = \frac{\alpha_0}{n_i \Lambda_e^3} \exp\left[-\frac{f_Z(\rho, T)}{kT}\right], \quad (7)$$

where the ion density is defined as $n_i = \rho / A_{\text{CH}}$, the electron’s thermal de Brogile wavelength is $\Lambda_e = h / \sqrt{2\pi m_e kT}$, with the

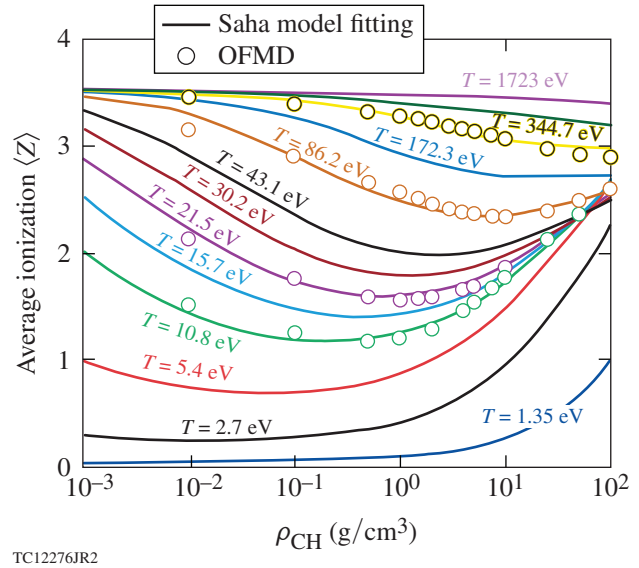


Figure 145.21

The OFMD-predicted average ionization $\langle Z \rangle$ as a function of CH density for plasma temperatures varying from $T \simeq 10.8$ eV to $T \simeq 344.7$ eV, which are fitted with the “Saha-type” ionization model described by Eq. (7).

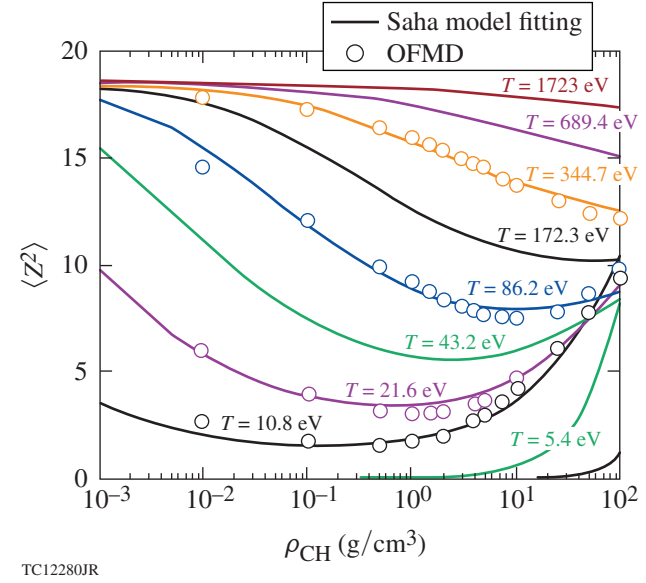


Figure 145.22

The OFMD-predicted average ionization square $\langle Z^2 \rangle$ as a function of CH density for plasma temperatures varying from $T \simeq 10.8$ eV to $T \simeq 344.7$ eV, which are fitted with the Saha-type ionization model described by Eq. (9).

Planck constant h and the electron mass m_e , and the density–temperature-dependent average-ionization potential has the following form (kT in eV):

$$f_Z(\rho, T) = \alpha_1 + \alpha_2 \times kT \times \left[\left(1 + \sqrt{3\Gamma_0} \right)^{1/4} - 1 \right] \\ + \alpha_3 \times (kT)^{0.9} + kT \times \left(\frac{\alpha_4}{r_0} + \frac{\alpha_5}{r_0^2} + \frac{\alpha_6}{r_0^3} \right) \quad (8)$$

with seven fitting parameters α_i . In Eq. (8), the second term accounts for the continuum lowering in the plasma similar to the Stewart–Pyatt form,⁵⁰ while the last term is for the pressure ionization. In Eq. (8), the ion–ion interdistance r_0 in terms of the Bohr radius α_B is defined as $n_i = \rho / A_{\text{CH}}$ and $r_0 = (1/\alpha_B)(3/4\pi n_i)^{1/3}$ with the ion density n_i . The average atomic weight $A_{\text{CH}} = (A_C + A_H)/2$ is used for CH. The quantity Γ_0 is proportional to the ion–ion coupling parameter, i.e., $\Gamma_0 = 1/r_0 kT$. Finally, the average ionization is expressed as $\langle Z \rangle = Z_{\text{max}} \times \xi$ with the maximum ionization of $Z_{\text{max}} = 3.5$ for the equal mixture of C and H. Performing a least-square fitting to the OFMD data with the above Saha model, we determined the following fitting parameters: $\alpha_0 = 87.222$, $\alpha_1 = 10.866$, $\alpha_2 = -28.412$, $\alpha_3 = 17.915$, $\alpha_4 = -2.422$, $\alpha_5 = 0.595$, and $\alpha_6 = -2.369 \times 10^{-2}$. The fitting is shown by lines in Fig. 145.21 for different temperatures varying from $T \simeq 1.35$ eV to $T \simeq 1723$ eV.

For the average ionization square $\langle Z^2 \rangle$, we adopted a similar model to fit the OFMD data, $\langle Z^2 \rangle = Z_{\text{max}}^2 \times \zeta$ with $Z_{\text{max}}^2 = 18.5$ for CH, and ζ is determined as

$$\frac{\zeta^2}{1 - \zeta} = \frac{\beta_0}{n_i \Lambda_e^3} \exp \left[-\frac{f_{Z^2}(\rho, T)}{kT} \right] \quad (9)$$

with a different fitting function

$$f_{Z^2}(\rho, T) = \beta_1 + \beta_2 \times kT \times \left[\left(1 + \sqrt{3\Gamma_0} \right)^{2/5} - 1 \right] + \beta_3 \\ \times (kT)^{3/4} + kT \times \left(\frac{\beta_4}{\sqrt{r_0}} + \frac{\beta_5}{r_0} + \frac{\beta_6}{r_0^{3/2}} + \frac{\beta_7}{r_0^2} \right). \quad (10)$$

The best fit to the OFMD results yielded the following parameters: $\beta_0 = 2.055 \times 10^{-3}$, $\beta_1 = 27.851$, $\beta_2 = -5.087$, $\beta_3 = 6.018$, $\beta_4 = -7.908$, $\beta_5 = 4.421$, $\beta_6 = -2.893$, and $\beta_7 = 0.961$. The model fitting of $\langle Z^2 \rangle$ is illustrated in Fig. 145.22 by colored lines, which all compared well with the OFMD results. With a fit for both $\langle Z \rangle$ and $\langle Z^2 \rangle$, we can now derive the effective charge of CH plasmas by $Z_{\text{eff}} = \langle Z^2 \rangle / \langle Z \rangle$ over a wide range of plasma conditions.

2. Thermal Conductivity κ_{QMD} of CH

Using the KSMD calculations with Eq. (3), we have calculated the thermal conductivity of CH plasmas for densities ranging from $\rho = 0.5$ g/cm³ to $\rho = 100$ g/cm³. For each density point, the κ_{QMD} calculations have been performed to the highest temperature approaching $T \simeq T_F$ [the Fermi temperature $T_F = \hbar^2/2mk \times (3\pi^2 n_e)^{2/3}$]. To test the effects of κ_{QMD} on ICF implosions, these results must be fitted in an analytical form. Similar to what we did for the deuterium case,²⁹ the following function is used for the fitting (in a similar format of κ_{LILAC} currently used in our hydrocode *LILAC*):⁵¹

$$\kappa_{\text{QMD}} = \frac{20 \times (2/\pi)^{3/2} k^{7/2} T^{5/2}}{\sqrt{m_e} e^4 Z_{\text{eff}}} \\ \times \frac{0.095 \times (Z_{\text{eff}} + 0.24)}{1 + 0.24 Z_{\text{eff}}} \times \frac{1}{(\ln \Lambda)_{\text{QMD}}}, \quad (11)$$

with the same Spitzer prefactor as used in κ_{LILAC} . Z_{eff} is the effective charge of CH plasmas that was determined in **The Average Ionization $\langle Z \rangle$ and $\langle Z^2 \rangle$ of CH**, p. 21. The generalized QMD Coulomb logarithm is a sixth-order polynomial function of ion–ion coupling and electron degeneracy parameters (Γ_i , θ_e), which has the following form:

$$(\ln \Lambda)_{\text{QMD}} = \exp \left\{ \gamma_0 + \sum_{j=1}^6 [\gamma_j (\ln \Gamma_i)^j + \sigma_j (\ln \theta_e)^j] \right\}, \quad (12)$$

with $\Gamma_i = \langle Z^2 \rangle e^2 / r_S kT$ and $\theta_e = T / T_F$, in which the Wigner–Seitz radius is defined as $r_S = r_0 \times \alpha_B$ and the free-electron density of $n_e = n_i \times \langle Z \rangle$. Using a multivariable least-square fitting to the κ_{QMD} data, we can determine the parameters γ_j and σ_j . To smoothly merge the κ_{QMD} results to the classical ideal plasma conditions ($\Gamma_i \ll 1$ and $\theta_e \gg 1$), we have added high-temperature κ_{LILAC} points into the dataset for the global fitting. The resulting fitting parameters are $\gamma_0 = -0.482$, $\gamma_1 = -0.150$ or $+0.275$, $\gamma_2 = +0.193$, $\gamma_3 = +8.364 \times 10^{-3}$, $\gamma_4 = -5.287 \times 10^{-3}$, $\gamma_5 = -3.191 \times 10^{-4}$, $\gamma_6 = +2.666 \times 10^{-5}$, $\sigma_1 = +1.00$ or $+1.20$, $\sigma_2 = -0.225$, $\sigma_3 = -4.652 \times 10^{-3}$, $\sigma_4 = +3.805 \times 10^{-3}$, $\sigma_5 = -7.643 \times 10^{-5}$, and $\sigma_6 = -1.391 \times 10^{-5}$. The choice for the two values of γ_1 and σ_1 , either $(\gamma_1, \sigma_1) = (-0.15, 1.0)$ or $(\gamma_1, \sigma_1) = (0.275, 1.2)$, is to minimize the Coulomb logarithm for a better fit to the QMD results. The fitting results of $(\ln \Lambda)_{\text{QMD}}$ are plotted in Figs. 145.23(a) and 145.23(b) as functions of $\ln(\Gamma_i)$ and $\ln(\theta_e)$, respectively. Overall, the global fitting with the above parameters gives only a small error of 5% or less.

Figures 145.24 and 145.25 compare the QMD-based thermal conductivities of CH plasmas with other models. The “hybrid” Lee–More model (κ_{LILAC}), which combined the Spitzer prefactor with the Lee–More Coulomb logarithm, is currently adopted in our hydrocode *LILAC*. The two others are the Ichimaru model⁵² for dense plasmas and the Hubbard model⁵³ for fully degenerate electron gases. Figure 145.24 compares κ_{QMD} with the different model predictions as a func-

tion of plasma temperature for CH densities of $\rho = 1.05 \text{ g/cm}^3$ (solid density) and $\rho = 4.0 \text{ g/cm}^3$ (shocked CH). It is seen that κ_{QMD} is generally larger than κ_{LILAC} by a factor of ~ 2 to 10 at $T < 20 \text{ eV}$. As indicated in Fig. 145.24(b), the Hubbard model gives reasonably good results in the low- T regime, where the electron degeneracy effect dominates transport behavior, while the Ichimaru model gives the correct trend for plasma temperatures approaching T_F and above. As seen in Fig. 145.23,

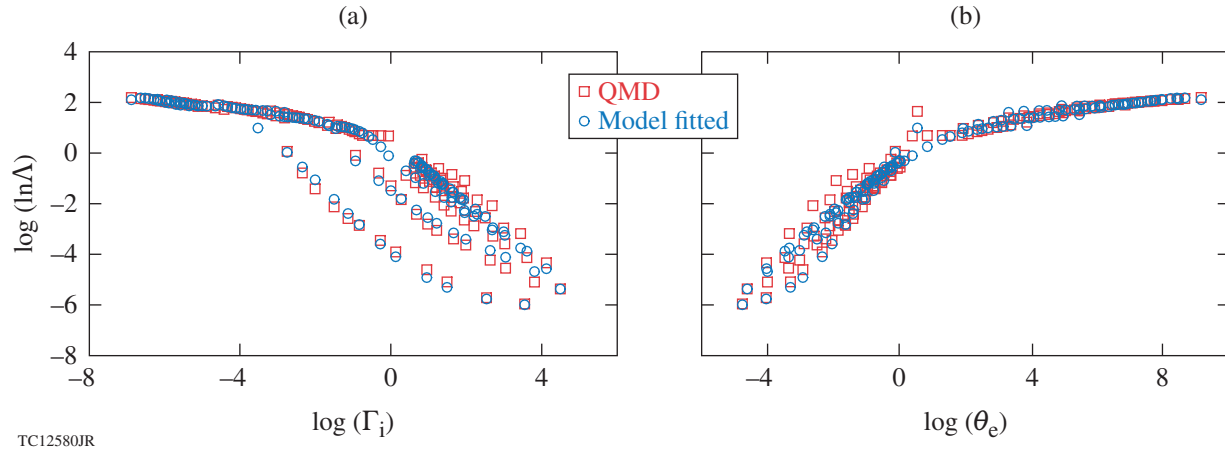


Figure 145.23

The generalized Coulomb logarithm, derived from QMD calculations of thermal conductivity, is fitted with a polynomial function of (a) the ion–ion coupling parameter (Γ_i) and (b) the electron degeneracy parameter (θ_e) of CH plasmas [Eq. (12)].

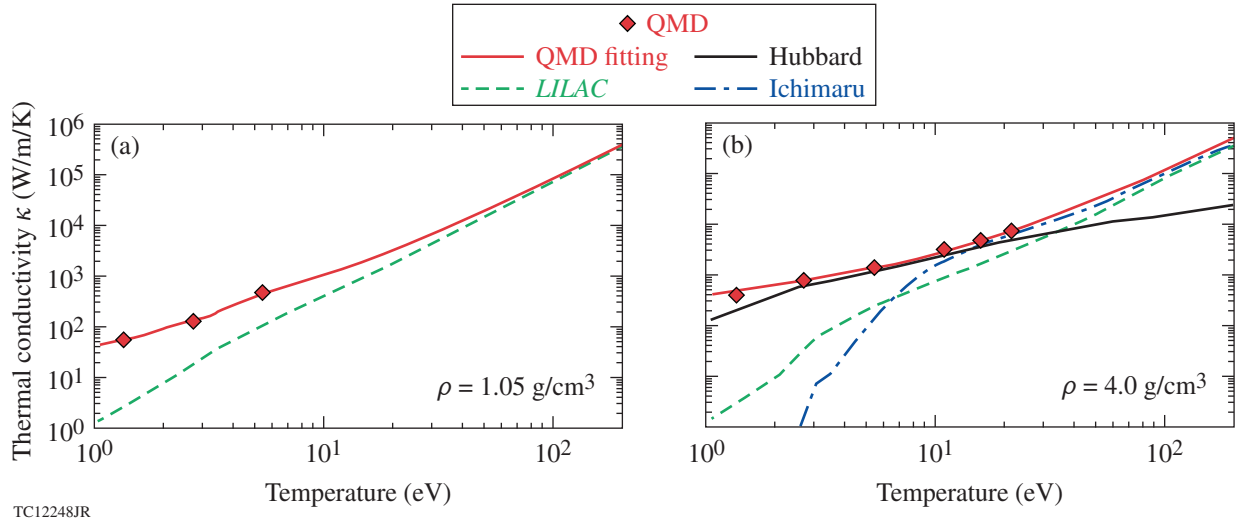


Figure 145.24

Comparison of thermal conductivities of CH plasmas as functions of temperature between QMD calculations and different thermal-conductivity models, for CH densities of (a) $\rho = 1.05 \text{ g/cm}^3$ and (b) $\rho = 4.0 \text{ g/cm}^3$. The hybrid *LILAC* model (green dashed lines) used in our hydrocodes adopted the Lee–More model for the Coulomb logarithm with a Spitzer prefactor. The Hubbard model was based on fully degenerate electron gas, while the Ichimaru model considered microfield corrections in dense plasmas.

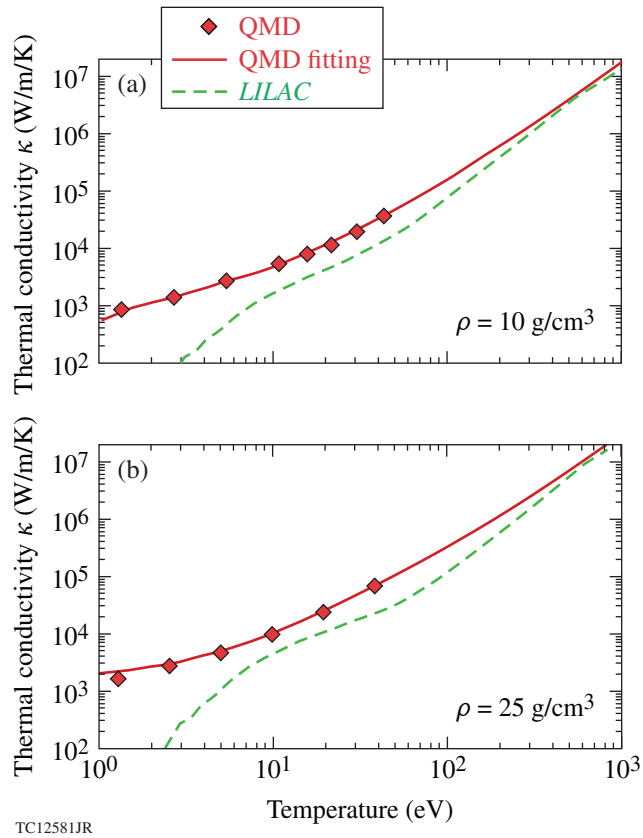


Figure 145.25

Similar to Fig. 145.24 but for CH densities of (a) $\rho = 10 \text{ g/cm}^3$ and (b) $\rho = 25 \text{ g/cm}^3$.

strongly coupled and degenerate plasmas ($\Gamma_i > 1$ and $\theta_e < 1$) lead to a smaller effective Coulomb logarithm that characterizes the electron collisions in plasmas, while the Lee–More model usually sets a minimum floor of $(\ln \Lambda)_{\min} = 2$. The decrease in $(\ln \Lambda)_{\text{QMD}}$ means a larger mean free path for electrons, thereby leading to higher thermal conductivity in QMD calculations that account for coupling and degeneracy effects in warm dense CH plasmas. Figures 145.25(a) and 145.25(b) show similar comparisons for higher CH densities at $\rho = 10 \text{ g/cm}^3$ and $\rho = 25 \text{ g/cm}^3$, respectively. Overall, it is seen that our current hybrid Lee–More model (κ_{LILAC}) underestimates the electronic thermal conductivity when compared with κ_{QMD} in the warm dense plasma regime. The enhancement of κ in the warm dense CH plasmas may have implications in ICF simulations.

The Effect of κ_{QMD} on ICF Simulations

With the implementation of both Z_{eff} and κ_{QMD} into the hydrocode *LILAC* through the fitting formulas discussed above, their effects on ICF simulations may be examined. We

first simulate a typical cryogenic DT implosion on OMEGA. Figure 145.26 shows the triple-picket laser pulse used for the implosion, while the inset illustrates the target dimensions. The cryogenic DT target on OMEGA has a 40- μm -thick DT ice layer covered by a 7.5- μm -thick deuterated-plastic (CD) ablator. The total target radius is $\sim 432.5 \mu\text{m}$. In the simulations a density scaling to obtain κ_{QMD} for CD from the above-derived κ_{QMD} for CH is used. The triple-picket pulse shape has been used extensively for implosions on OMEGA,^{54–56} which enables one to better control shock timing.^{57,58}

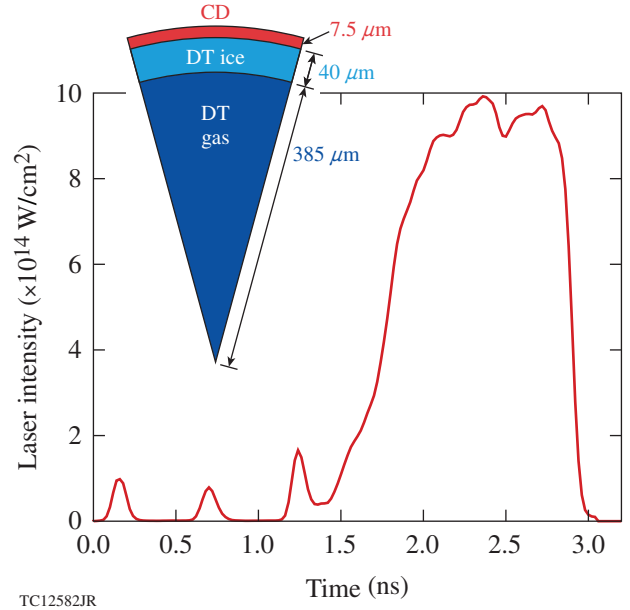


Figure 145.26

The pulse shape and target dimension for a typical cryogenic DT target implosion on OMEGA.

The 1-D *LILAC* hydro simulation results are displayed in Fig. 145.27. Figure 145.27(a) compares density profiles between the κ_{QMD} simulation and the traditional κ_{LILAC} simulation at the end of the laser pulse ($t = 2.96 \text{ ns}$). At this time the thin CD layer has been ablated away from the shell. The density of the imploding DT shell is plotted as a function of target radius. One sees that the κ_{QMD} simulation (solid red line) predicts the DT shell being behind the κ_{LILAC} case (DT shell is moving inward); the κ_{QMD} simulation also gives a slightly lower density than the κ_{LILAC} simulation. In the two simulations, we have kept all inputs the same except for the different thermal-conductivity model. Namely, we have employed the FPEOS for both CH¹⁹ and DT,⁵⁹ the first-principles opacity table for DT,⁴⁹ and a flux-limiter model for thermal transport. The larger value of κ_{QMD} causes more heat to flow into the high-density CD layer, while

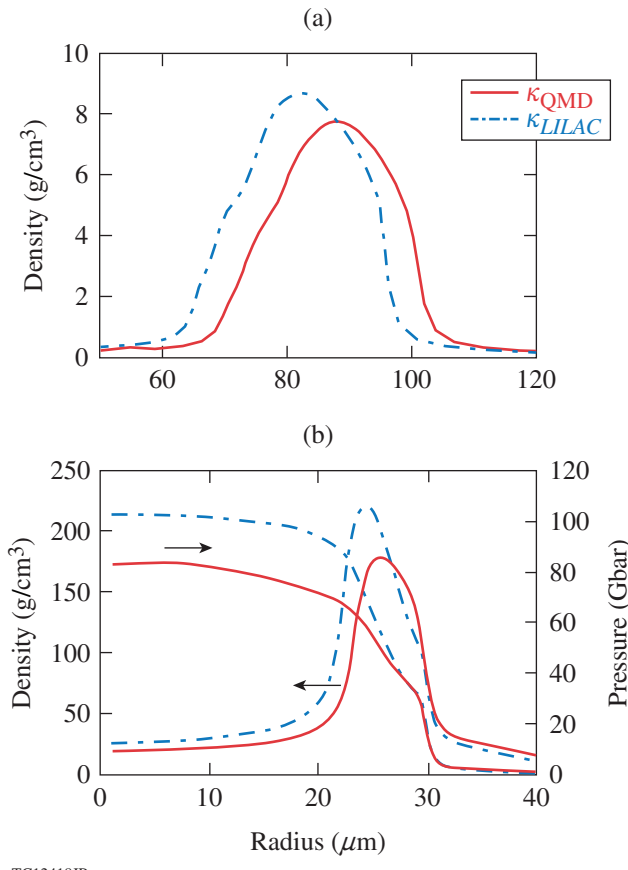


Figure 145.27

Comparison of density profiles and hot-spot pressures predicted by two hydrodynamic simulations using the new κ_{QMD} (red solid lines) and the traditional κ_{LILAC} (blue dashed-dotted lines), respectively. (a) The end of the pulse ($t = 2.96 \text{ ns}$) and (b) the implosion reaching its peak neutron production ($t = 3.14 \text{ ns}$). The overall target performances are compared in Table 145.III.

the electron temperature is reduced somewhat between the ablation front and the conduction zone when compared to the κ_{LILAC} case. This reduces the ablation efficiency, thereby leading to a slightly slower implosion. When the DT shell stagnates at $t = 3.14 \text{ ns}$, the two simulations lead to certain differences in target performance. The comparisons are made in Fig. 145.27(b) for both peak densities in the shell and pressures in the hot spot. The peak density drops from $\rho_p \simeq 220 \text{ g}/\text{cm}^3$ predicted by the κ_{LILAC} simulation to $\rho_p \simeq 180 \text{ g}/\text{cm}^3$ in the κ_{QMD} simulation. Also, the hot-spot peak pressure decreases from $P \simeq 105 \text{ Gbar}$ (κ_{LILAC}) to $P \simeq 84 \text{ Gbar}$ (κ_{QMD}). Table 145.III summarizes the overall comparison in target performance from the two simulations with a variation in yield of $\sim 20\%$.

The effects of κ_{QMD} are tested for a symmetric direct-drive–ignition design on the NIF, as seen in Figs. 145.28 and

145.29. The pulse shape is shown in Fig. 145.28, which is hydro-equivalently scaled from the above OMEGA target. It consists of a 180- μm -thick DT layer with a 35- μm CD ablator. The target diameter is about 3.43 mm, illustrated by the inset in Fig. 145.28. Results from the two simulations are shown in Fig. 145.29 for comparison. Figure 145.29(a) displays the DT shell’s density as a function of target radius for both κ_{LILAC} (blue dashed–dotted line) and κ_{QMD} (red solid line) simulations. Similar to what was found for the implosion case on OMEGA, the NIF simulation using κ_{QMD} also indicates a slight slowdown in the implosion. This causes the difference seen in Fig. 145.29(b) at the start of the ignition burn. The comparison in target performance is summarized in Table 145.IV.

Table 145.III: Comparison of target performance of a typical cryogenic DT implosion on OMEGA simulated with κ_{QMD} versus κ_{LILAC} of CD. The subscript “n” represents neutron-averaged quantities.

OMEGA	κ_{LILAC}	κ_{QMD}
Yield	1.9×10^{14}	1.6×10^{14}
P_{peak}	105 Gbar	84 Gbar
$\langle T_i \rangle_n$	4.17 keV	4.07 keV
$\langle P \rangle_n$	78 Gbar	72 Gbar
$\langle \rho R \rangle_n$	213 mg/cm ²	208 mg/cm ²

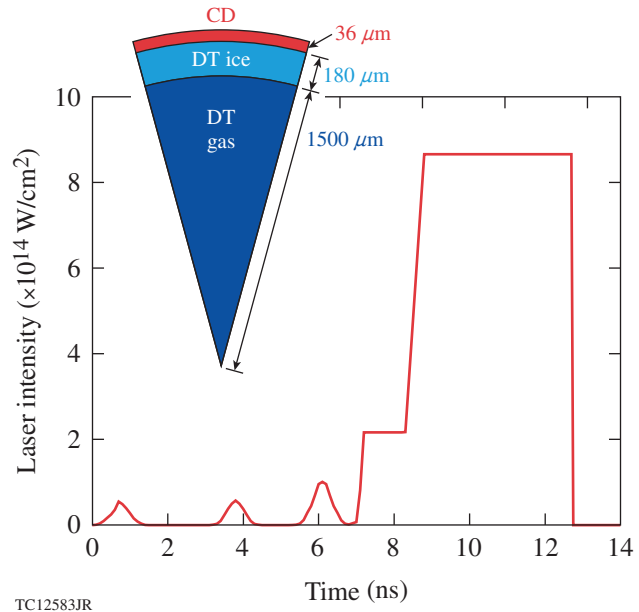


Figure 145.28

The pulse shape and target dimension for a symmetrical ignition design on the NIF.

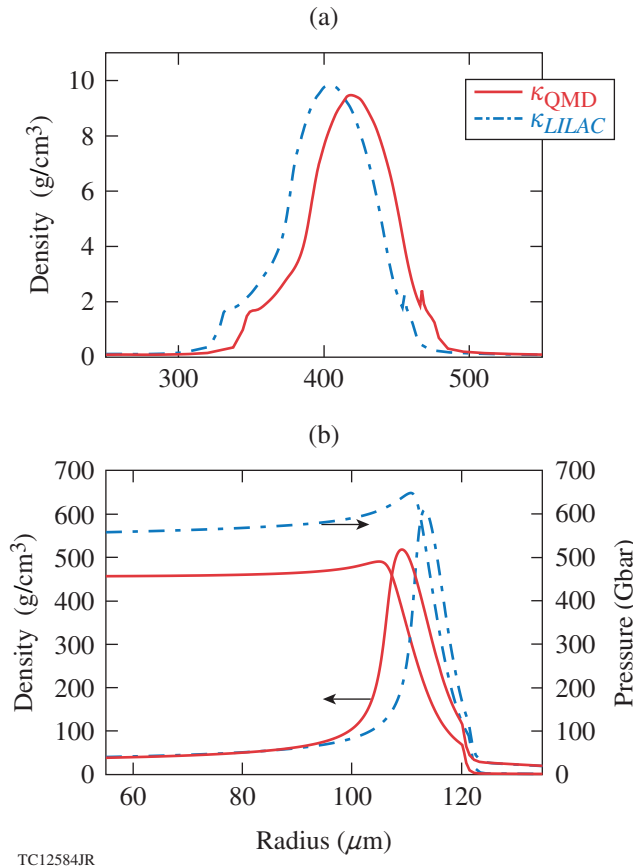


Figure 145.29

Simulation comparison of the NIF design in Fig. 145.28 using the new κ_{QMD} (red solid lines) and the traditional κ_{LILAC} (blue dashed-dotted lines), respectively. (a) The predicted density profiles at the peak velocity ($t = 13$ ns) and (b) hot-spot pressure and peak shell density compared for the two cases at $t = 14$ ns. The overall target performance is compared in Table 145.IV.

Table 145.IV: Comparison of a NIF ignition design simulated with κ_{QMD} versus κ_{LILAC} for CD.

NIF	κ_{LILAC}	κ_{QMD}
$\langle \rho R \rangle_n$	0.814 g/cm ²	0.786 g/cm ²
$\langle T_i \rangle_n$	20.8 keV	19.1 keV
$\langle P \rangle_n$	629 Gbar	546 Gbar
$\langle \rho \rangle_{\text{peak}}$	639.6 g/cm ³	586.6 g/cm ³
$R_{\text{hot spot}}$	74.1 μm	78.5 μm
$C_{\text{hot spot}}$	23.2	21.8
Yield	1.85×10^{19}	1.62×10^{19}
Gain	35	30

The target performance is overall degraded in the κ_{QMD} simulation when compared with the predictions from the traditional κ_{LILAC} simulation. The κ_{QMD} simulation predicts that the hot-spot radius $R_{\text{hot spot}}$ is slightly bigger and the hot-spot convergence ratio $C_{\text{hot spot}}$ decreases relative to the κ_{LILAC} case. The final gain is reduced by $\sim 15\%$ in the κ_{QMD} simulation.

Conclusion

Combining the first-principles methods of KSMD and OFMD, the ionization and thermal conductivity of CH plasmas for a wide range of ICF plasma conditions were investigated. The derived average ionization from OFMD calculations has large discrepancies with respect to the astrophysics model predictions in warm dense CH plasmas. The global behavior of $\langle Z \rangle$ and $\langle Z^2 \rangle$ has been fitted with a proposed Saha-type ionization model, which takes the continuum lowering and pressure ionization into account. The derived effective charge $Z_{\text{eff}} = \langle Z^2 \rangle / \langle Z \rangle$ is then applied to the global fitting of thermal conductivities κ_{QMD} of CH plasmas, using a generalized Coulomb logarithm $(\ln \Lambda)_{\text{QMD}}$. The QMD-based models of Z_{eff} and κ_{QMD} are implemented into our hydrocode for ICF simulations. Compared with the traditional simulations using AOT-based Z_{eff} and κ_{LILAC} , the new simulations with QMD-based Z_{eff} and κ_{QMD} have shown a 15% to $\sim 20\%$ reduction in target performance (yield and energy gain) for both OMEGA and NIF implosions. It is anticipated that these plasma properties of CH, derived from first-principles calculations, will improve the predictions of ICF implosions and other HEDP experiments involving CH ablators. It may also further stimulate the ongoing experimental efforts to measure thermal conductivity in high-energy-density plasmas.⁶⁰

ACKNOWLEDGMENT

This material is based upon work supported by the Department of Energy National Nuclear Security Administration under Award Number DE-NA0001944, the University of Rochester, and the New York State Energy Research and Development Authority. The support of DOE does not constitute an endorsement by DOE of the views expressed in this article. This work was also supported by Scientific Campaign 10 at the Los Alamos National Laboratory, operated by Los Alamos National Security, LLC, for the National Nuclear Security Administration of the U.S. Department of Energy under Contract No. DE-AC52-06NA25396.

REFERENCES

1. S. W. Haan *et al.*, Phys. Plasmas **18**, 051001 (2011).
2. M. J. Edwards, J. D. Lindl, B. K. Spears, S. V. Weber, L. J. Atherton, D. L. Bleuel, D. K. Bradley, D. A. Callahan, C. J. Cerjan, D. Clark, G. W. Collins, J. E. Fair, R. J. Fortner, S. H. Glenzer, S. W. Haan, B. A. Hammel, A. V. Hamza, S. P. Hatchett, N. Izumi, B. Jacoby, O. S. Jones, J. A. Koch, B. J. Kozioziemski, O. L. Landen, R. Lerche, B. J. MacGowan, A. J. MacKinnon, E. R. Mapoles, M. M. Marinak,

- M. Moran, E. I. Moses, D. H. Munro, D. H. Schneider, S. M. Sepke, D. A. Shaughnessy, P. T. Springer, R. Tommasini, L. Bernstein, W. Stoeffl, R. Betti, T. R. Boehly, T. C. Sangster, V. Yu. Glebov, P. W. McKenty, S. P. Regan, D. H. Edgell, J. P. Knauer, C. Stoeckl, D. R. Harding, S. Batha, G. Grim, H. W. Herrmann, G. Kyrala, M. Wilke, D. C. Wilson, J. Frenje, R. Petrasso, K. Moreno, H. Huang, K. C. Chen, E. Giraldez, J. D. Kilkenny, M. Mauldin, N. Hein, M. Hoppe, A. Nikroo, and R. J. Leeper, Phys. Plasmas **18**, 051003 (2011).
3. C. Cherfils-Clérouin *et al.*, J. Phys.: Conf. Ser. **244**, 022009 (2010).
 4. D. D. Meyerhofer, R. L. McCrory, R. Betti, T. R. Boehly, D. T. Casey, T. J. B. Collins, R. S. Craxton, J. A. Delettrez, D. H. Edgell, R. Epstein, K. A. Fletcher, J. A. Frenje, V. Yu. Glebov, V. N. Goncharov, D. R. Harding, S. X. Hu, I. V. Igumenshchev, J. P. Knauer, C. K. Li, J. A. Marozas, F. J. Marshall, P. W. McKenty, P. M. Nilson, S. P. Padalino, R. D. Petrasso, P. B. Radha, S. P. Regan, T. C. Sangster, F. H. Séguin, W. Seka, R. W. Short, D. Shvarts, S. Skupsky, J. M. Soures, C. Stoeckl, W. Theobald, and B. Yaakobi, Nucl. Fusion **51**, 053010 (2011).
 5. R. L. McCrory, R. Betti, T. R. Boehly, D. T. Casey, T. J. B. Collins, R. S. Craxton, J. A. Delettrez, D. H. Edgell, R. Epstein, J. A. Frenje, D. H. Froula, M. Gatou-Johnson, V. Yu. Glebov, V. N. Goncharov, D. R. Harding, M. Hohenberger, S. X. Hu, I. V. Igumenshchev, T. J. Kessler, J. P. Knauer, C. K. Li, J. A. Marozas, F. J. Marshall, P. W. McKenty, D. D. Meyerhofer, D. T. Michel, J. F. Myatt, P. M. Nilson, S. J. Padalino, R. D. Petrasso, P. B. Radha, S. P. Regan, T. C. Sangster, F. H. Séguin, W. Seka, R. W. Short, A. Shvydky, S. Skupsky, J. M. Soures, C. Stoeckl, W. Theobald, B. Yaakobi, and J. D. Zuegel, Nucl. Fusion **53**, 113021 (2013).
 6. R. S. Craxton, K. S. Anderson, T. R. Boehly, V. N. Goncharov, D. R. Harding, J. P. Knauer, R. L. McCrory, P. W. McKenty, D. D. Meyerhofer, J. F. Myatt, A. J. Schmitt, J. D. Sethian, R. W. Short, S. Skupsky, W. Theobald, W. L. Kruer, K. Tanaka, R. Betti, T. J. B. Collins, J. A. Delettrez, S. X. Hu, J. A. Marozas, A. V. Maximov, D. T. Michel, P. B. Radha, S. P. Regan, T. C. Sangster, W. Seka, A. A. Solodov, J. M. Soures, C. Stoeckl, and J. D. Zuegel, Phys. Plasmas **22**, 110501 (2015).
 7. S. W. Haan, H. Huang, M. A. Johnson, M. Stadermann, S. Baxamusa, S. Bhandarkar, D. S. Clark, V. Smalyuk, and H. F. Robey, Phys. Plasmas **22**, 032708 (2015); T. C. Sangster, V. N. Goncharov, R. Betti, T. R. Boehly, D. T. Casey, T. J. B. Collins, R. S. Craxton, J. A. Delettrez, D. H. Edgell, R. Epstein, K. A. Fletcher, J. A. Frenje, V. Yu. Glebov, D. R. Harding, S. X. Hu, I. V. Igumenshchev, J. P. Knauer, S. J. Loucks, C. K. Li, J. A. Marozas, F. J. Marshall, R. L. McCrory, P. W. McKenty, D. D. Meyerhofer, P. M. Nilson, S. P. Padalino, R. D. Petrasso, P. B. Radha, S. P. Regan, F. H. Séguin, W. Seka, R. W. Short, D. Shvarts, S. Skupsky, V. A. Smalyuk, J. M. Soures, C. Stoeckl, W. Theobald, and B. Yaakobi, Phys. Plasmas **17**, 056312 (2010).
 8. S. H. Glenzer and R. Redmer, Rev. Mod. Phys. **81**, 1625 (2009).
 9. A. L. Kritcher *et al.*, Phys. Rev. Lett. **107**, 015002 (2011).
 10. L. B. Fletcher *et al.*, Phys. Rev. Lett. **112**, 145004 (2014).
 11. S. P. Marsh, ed. *LASL Shock Hugoniot Data*, Los Alamos Series on Dynamic Material Properties (University of California Press, Berkeley, CA, 1980).
 12. R. Cauble *et al.*, Phys. Plasmas **4**, 1857 (1997).
 13. N. Ozaki *et al.*, Phys. Plasmas **16**, 062702 (2009).
 14. M. Koenig *et al.*, Phys. Plasmas **10**, 3026 (2003).
 15. M. A. Barrios, D. G. Hicks, T. R. Boehly, D. E. Fratanduono, J. H. Eggert, P. M. Celliers, G. W. Collins, and D. D. Meyerhofer, Phys. Plasmas **17**, 056307 (2010).
 16. S. Hamel, L. X. Benedict, P. M. Celliers, M. A. Barrios, T. R. Boehly, G. W. Collins, T. Döppner, J. H. Eggert, D. R. Farley, D. G. Hicks, J. L. Kline, A. Lazicki, S. LePape, A. J. Mackinnon, J. D. Moody, H. F. Robey, E. Schwegler, and P. A. Sterne, Phys. Rev. B **86**, 094113 (2012).
 17. C. Wang, X.-T. He, and P. Zhang, Phys. Plasmas **18**, 082707 (2011).
 18. S. X. Hu, T. R. Boehly, and L. A. Collins, Phys. Rev. E **89**, 063104 (2014).
 19. S. X. Hu, L. A. Collins, V. N. Goncharov, J. D. Kress, R. L. McCrory, and S. Skupsky, Phys. Rev. E **92**, 043104 (2015).
 20. B. A. Hammel *et al.*, High Energy Density Phys. **6**, 171 (2010).
 21. L. Spitzer, Jr. and R. Härm, Phys. Rev. **89**, 977 (1953).
 22. Y. T. Lee and R. M. More, Phys. Fluids **27**, 1273 (1984).
 23. B. Wilson *et al.*, J. Quant. Spectrosc. Radiat. Transf. **99**, 658 (2006).
 24. G. Faussurier *et al.*, Phys. Plasmas **17**, 052707 (2010); J. Clérouin *et al.*, Phys. Rev. E **82**, 046402 (2010).
 25. V. Recoules *et al.*, Phys. Rev. Lett. **102**, 075002 (2009).
 26. F. Lambert *et al.*, Phys. Plasmas **18**, 056306 (2011).
 27. B. Holst, M. French, and R. Redmer, Phys. Rev. B **83**, 235120 (2011).
 28. C. Wang *et al.*, Phys. Rev. E **88**, 013106 (2013).
 29. S. X. Hu, L. A. Collins, T. R. Boehly, J. D. Kress, V. N. Goncharov, and S. Skupsky, Phys. Rev. E **89**, 043105 (2014).
 30. F. Lambert and V. Recoules, Phys. Rev. E **86**, 026405 (2012).
 31. C. E. Starrett *et al.*, Phys. Plasmas **19**, 102709 (2012).
 32. D. V. Knyazev and P. R. Levashov, Phys. Plasmas **22**, 053303 (2015).
 33. L. Collins *et al.*, Phys. Rev. E **52**, 6202 (1995).
 34. J. G. Clérouin and S. Bernard, Phys. Rev. E **56**, 3534 (1997).
 35. L. A. Collins *et al.*, Phys. Rev. B **63**, 184110 (2001).
 36. M. P. Desjarlais, Phys. Rev. B **68**, 064204 (2003).
 37. P. Hohenberg and W. Kohn, Phys. Rev. **136**, B864 (1964).
 38. W. Kohn and L. J. Sham, Phys. Rev. **140**, A1133 (1965).
 39. N. D. Mermin, Phys. Rev. **137**, A1441 (1965).
 40. G. Kresse and J. Hafner, Phys. Rev. B **47**, 558 (1993).

41. G. Kresse and J. Hafner, Phys. Rev. B **49**, 14,251 (1994).
42. G. Kresse and J. Furthmüller, Phys. Rev. B **54**, 11,169 (1996).
43. F. Lambert, J. Clérouin, and G. Zérah, Phys. Rev. E **73**, 016403 (2006).
44. J. P. Perdew, K. Burke, and M. Ernzerhof, Phys. Rev. Lett. **77**, 3865 (1996); **78**, 1396(E) (1997).
45. R. Kubo, J. Phys. Soc. Jpn. **12**, 570 (1957).
46. D. A. Greenwood, Proc. Phys. Soc. Lond. **71**, 585 (1958).
47. F. Lambert *et al.*, Phys. Rev. E **77**, 026402 (2008).
48. W. F. Huebner *et al.*, Los Alamos National Laboratory, Los Alamos, NM, Report LA-6760-M (1977).
49. S. X. Hu, L. A. Collins, V. N. Goncharov, T. R. Boehly, R. Epstein, R. L. McCrory, and S. Skupsky, Phys. Rev. E **90**, 033111 (2014).
50. J. C. Stewart and K. D. Pyatt, Jr., Astrophys. J. **144**, 1203 (1966).
51. J. Delettrez, R. Epstein, M. C. Richardson, P. A. Jaanimagi, and B. L. Henke, Phys. Rev. A **36**, 3926 (1987).
52. S. Ichimaru and S. Tanaka, Phys. Rev. A **32**, 1790 (1985); H. Kitamura and S. Ichimaru, Phys. Rev. E **51**, 6004 (1995).
53. W. B. Hubbard, Astrophys. J. **146**, 858 (1966).
54. V. N. Goncharov, T. C. Sangster, T. R. Boehly, S. X. Hu, I. V. Igumenshchev, F. J. Marshall, R. L. McCrory, D. D. Meyerhofer, P. B. Radha, W. Seka, S. Skupsky, C. Stoeckl, D. T. Casey, J. A. Frenje, and R. D. Petrasso, Phys. Rev. Lett. **104**, 165001 (2010).
55. S. X. Hu, V. N. Goncharov, P. B. Radha, J. A. Marozas, S. Skupsky, T. R. Boehly, T. C. Sangster, D. D. Meyerhofer, and R. L. McCrory, Phys. Plasmas **17**, 102706 (2010).
56. T. C. Sangster, V. N. Goncharov, R. Betti, P. B. Radha, T. R. Boehly, D. T. Casey, T. J. B. Collins, R. S. Craxton, J. A. Delettrez, D. H. Edgell, R. Epstein, C. J. Forrest, J. A. Frenje, D. H. Froula, M. Gatu-Johnson, V. Yu. Glebov, D. R. Harding, M. Hohenberger, S. X. Hu, I. V. Igumenshchev, R. Janezic, J. H. Kelly, T. J. Kessler, C. Kingsley, T. Z. Kosc, J. P. Knauer, S. J. Loucks, J. A. Marozas, F. J. Marshall, A. V. Maximov, R. L. McCrory, P. W. McKenty, D. D. Meyerhofer, D. T. Michel, J. F. Myatt, R. D. Petrasso, S. P. Regan, W. Seka, W. T. Shmayda, R. W. Short, A. Shvydky, S. Skupsky, J. M. Soures, C. Stoeckl, W. Theobald, V. Versteeg, B. Yaakobi, and J. D. Zuegel, Phys. Plasmas **20**, 056317 (2013).
57. T. R. Boehly, V. N. Goncharov, W. Seka, S. X. Hu, J. A. Marozas, D. D. Meyerhofer, P. M. Celliers, D. G. Hicks, M. A. Barrios, D. Fratanduono, and G. W. Collins, Phys. Plasmas **18**, 092706 (2011).
58. H. F. Robey, J. D. Moody, P. M. Celliers, J. S. Ross, J. Ralph, S. Le Pape, L. Berzak Hopkins, T. Parham, J. Sater, E. R. Mapoles, D. M. Holunga, C. F. Walters, B. J. Haid, B. J. Koziolinski, R. J. Dylla-Spears, K. G. Krauter, G. Frieders, G. Ross, M. W. Bowers, D. J. Strozzi, B. E. Yoxall, A. V. Hamza, B. Dzenitis, S. D. Bhandarkar, B. Young, B. M. Van Wonterghem, L. J. Atherton, O. L. Landen, M. J. Edwards, and T. R. Boehly, Phys. Rev. Lett. **111**, 065003 (2013).
59. S. X. Hu, B. Militzer, V. N. Goncharov, and S. Skupsky, Phys. Rev. Lett. **104**, 235003 (2010); S. X. Hu, B. Militzer, V. N. Goncharov, and S. Skupsky, Phys. Rev. B **84**, 224109 (2011).
60. Y. Ping, A. Fernandez-Panella, H. Sio, A. Correa, R. Shepherd, O. Landen, R. A. London, P. A. Sterne, H. D. Whitley, D. Fratanduono, T. R. Boehly, and G. W. Collins, Phys. Plasmas **22**, 092701 (2015).